

Time-lapse wave-equation inversion

Gboyega Ayeni and Biondo Biondi

ABSTRACT

A regularized least-squares inversion scheme is proposed as a method for correcting poor and uneven subsurface illumination under complex overburden and for attenuating image differences resulting from differences in acquisition geometries. This approach involves a joint inversion of migrated images from different vintages with filters that are explicitly derived from the Hessian of the least-squares solution to the linearized wave equation. By using such a formulation, both the imaging and monitoring challenges are solved as a single problem that yields a more accurate image of the subsurface and its time-evolution. Numerical tests show that this joint inversion technique yields more accurate time-lapse images than those obtained by differencing independently migrated or inverted images.

INTRODUCTION

Time-lapse (4D) seismic is based on the premise that changes in reservoir fluid content (associated with production) cause changes in the acoustic properties of rocks and that such changes are detectable in recorded seismic data. Recent developments in seismic acquisition and imaging, and improved understanding of the relationships between seismic data and rock/fluid properties have contributed to the successes in applications of time-lapse seismic to hydrocarbon reservoir monitoring. Although time-lapse imaging of conventional reservoirs is now a mature technology, there has been little success reported in regions of complex geology (e.g., subsalt reservoirs), or in areas where acquisition repeatability is difficult, expensive, or impossible (e.g., because of latter development facilities between surveys).

In recent years, emphasis has been placed on developing better acquisition systems (to ensure high repeatability of surveys and high fidelity datasets) and processing schemes to better discriminate between the effects of reservoir changes from those attributable and unwanted noise. However, time-lapse seismic applications in relatively complex frontier areas, (e.g., deep-water Gulf of Mexico), have been limited mainly because of the imaging difficulties below the complex overburdens and the associated uneven illumination patterns. Also, rapid changes in acquisition techniques throughout the life of most reservoirs usually lead to datasets with different geometries, often causing considerably high-amplitude noise in the time-lapse image.

The proposed joint inversion method utilizes a system of non-stationary deconvolution filters derived from an explicit computation of a target-oriented, least-squares

Hessian of the linearized wave-equation (Valenciano et al., 2006). The inversion process attenuates distortions caused by uneven illumination and geometry differences. The joint inversion scheme enables incorporation of prior knowledge of the reservoir location, extent and geometry into the inversion as a form of model styling (or regularization). An important advantage of the proposed scheme over separate inversion is that different regularization goals can be established for the baseline and time-lapse changes during inversion. Outputs from this scheme include an inverted baseline image and its evolution through time (i.e., time-lapse difference images). A fundamental assumption in the current formulation is that the background baseline velocity model is known and that it does not change significantly between surveys. As opposed to schemes that attempt to directly recover velocity variations between surveys (e.g., Ajo-Franklin et al. (2005)), we assume that changes in reservoir properties can be recovered from the resulting time-lapse reflectivity images.

In this paper, we briefly describe time-lapse seismic monitoring (TLSM) practice and challenges, we summarize the basic idea of linear inversion, and then describe a joint inversion formulation — based on the simultaneous deconvolution of two or more surveys — that attenuates unwanted image differences. Finally, we demonstrate that the joint inversion scheme could be used to correct for both illumination and geometry differences using two synthetic datasets (one from Born single-scattering and the other from two-way variable-density acoustic modeling).

BACKGROUND

The acoustic properties of reservoir rocks are strongly influenced by the fluids stored in their pore spaces. Batzle and Wang (1992) discuss some of the most important seismic properties of reservoir fluids and how they influence seismic properties. Lumley (1995) and Calvert (2005) give comprehensive review of the theory, processing and applications of seismic monitoring. Since its adoption as a reservoir monitoring tool, many successful applications of TLSM have been reported (Lefeuvre et al., 2003; Whitcombe et al., 2004; Zou et al., 2006).

Repeatability is a major consideration for successful application of time-lapse seismic to reservoir monitoring, especially in formations with weak seismic responses, where imaged reservoir changes are subtle. Non-repeatability can result from differences in survey acquisition geometry and binning, cable feathering, tides, source-wavelet bandwidth and phase variability, differential static time-shifts, ambient noise, residual multiple energy, and relative mispositioning of imaged reflection events (Rickett and Lumley, 2001; Johnston, 2005). Laws and Kragh (2000) and Eiken et al. (2003) discuss acquisition techniques that reduce some of these uncertainties.

Some common time-lapse seismic processing schemes (which in general involve among other processes, spatial re-alignment, match filtering, amplitude balancing, and warping) and caveats have been discussed by several authors (Eastwood et al., 1994; Ross and Altan, 1997; Rickett and Lumley, 2001; Calvert, 2005; Johnston,

2005). Although advances in such processing methods have improved the success rate of TLSM, most methods fail in complex geological environments. One dominant reason for such failure is the uneven illumination that cause unreliable seismic amplitudes, thus precluding their use in TLSM. For the example of subsalt reservoirs, large contrasts at salt boundaries, complexity of seismic travel paths, and the associated complex and uneven illumination patterns (Muerdter and Ratcliff, 2001) are major hindrances to application of TLSM. Some recent acquisition techniques (e.g., wide-, rich- and full-azimuth, ocean-bottom, and virtual source surveys) improve imaging and illumination of reservoirs under complex overburdens (Korneev and Bakulin, 2006; Sava, 2006). Although, such acquisition methods, coupled with recent developments in wave-equation migration, have led more accurate images, they have seen limited applications in seismic monitoring in complex geology. The method discussed in this paper attempts to solve some of the monitoring challenges in these complex environments. The primary objective of the inversion scheme is to compensate for uneven subsurface illumination (and illumination differences when surveys have different geometries), while simultaneously optimizing the estimation of time-lapse changes between surveys.

Although some of the current best practices in TLSM improve the reliability of time-lapse responses and their interpretations, many limitations still exist. Most shortcomings are of lower importance in reservoirs with large seismic responses or low background noise — where such artifacts are submerged by the stronger time-lapse response. However, in many stiff reservoirs and those with complex or uneven illumination patterns (e.g., subsalt reservoirs), small inaccuracies can cause considerably large spurious 4D responses. We envisage that with the gradual increase in demand for more optimal reservoir management (hence the need for more accurate time-lapse amplitudes), and rapid changes in acquisition systems and techniques (hence the need to utilize surveys with potentially widely varying geometries for monitoring), new imaging and monitoring methods will be required to overcome the shortcomings in current time-lapse imaging practice. The need for such new methods is even more apparent with the gradual shift towards more complex exploration frontiers (e.g., deep-water Gulf of Mexico and deep-water West-Africa), where most current methods fail. With the general trend of increased speed of modern computers and the gradual drop in storage cost and computational memory, we believe a joint inversion scheme could be feasible for small- to medium-sized TLSM objectives in the immediate future.

Some authors have discussed joint inversion methods for time-lapse changes of certain reservoir properties. Sarkar et al. (2003) obtained more accurate estimates of changes in reservoir elastic parameters by a coupled impedance inversion of base and monitor datasets. Ajo-Franklin et al. (2005) attenuate some artifacts that persist in image differences from separately inverted datasets by solving a coupled tomographic inversion problem. Also, Zhang et al. (2005) show examples of simultaneous inversion for time-lapse changes using a convolutional model.

Although our primary objective is to invert for reflectivity amplitudes, it is possible to directly extend our formulation to changes in reservoir rock and fluid properties

(e.g., pressure and saturation), since there are known relationships between such properties and reflectivity (or impedance) amplitudes. An advantage of this method over those of Sarkar et al. (2003) and Zhang et al. (2005) is that most geometry and illumination artifacts are directly attenuated by the deconvolution operator. Also, we avoid making a constant wavelet assumption throughout (or over large regions) of the model space as is typical in many time-lapse inversion schemes.

In the following sections we discuss the basic theory of wave-equation inversion (and some approximations) and then introduce the joint inversion scheme as an alternative to current standard time-lapse processing methods. Then, using synthetic examples, we demonstrate how the technique could be used to attenuate geometry and illumination differences between two or multiple surveys.

THEORY

Linear inversion

Given a linear modeling operator \mathbf{L} , the seismic data \mathbf{d} can be computed as

$$\mathbf{L}\mathbf{m} = \mathbf{d}, \quad (1)$$

where \mathbf{m} is the reflectivity model. The modeling operator, \mathbf{L} , in this study, is an approximation to the seismic acquisition process. Two different surveys — say a baseline and monitor — acquired at different times ($\mathbf{t} = \mathbf{0}$ and $\mathbf{t} = \mathbf{1}$ respectively) over the same earth model can be represented as follows:

$$\begin{aligned} \mathbf{L}_0\mathbf{m}_0 &= \mathbf{d}_0, \\ \mathbf{L}_1\mathbf{m}_1 &= \mathbf{d}_1, \end{aligned} \quad (2)$$

where \mathbf{m}_0 and \mathbf{m}_1 are respectively the reflectivity models at the times when the datasets \mathbf{d}_0 and \mathbf{d}_1 were acquired, and \mathbf{L}_0 and \mathbf{L}_1 are the modeling operators that defining the acquisition process for the two surveys (a baseline and monitor). We assume that there is not a significant change in the background velocity within such time-interval as to significantly affect wave propagation. The quadratic cost functions for equation 2 are given by

$$\begin{aligned} S(\mathbf{m}_0) &= \|\mathbf{L}_0\mathbf{m}_0 - \mathbf{d}_0\|^2, \\ S(\mathbf{m}_1) &= \|\mathbf{L}_1\mathbf{m}_1 - \mathbf{d}_1\|^2, \end{aligned} \quad (3)$$

and the least-squares solutions are

$$\begin{aligned} \hat{\mathbf{m}}_0 &= (\mathbf{L}_0^\dagger\mathbf{L}_0)^{-1}\mathbf{L}_0^\dagger\mathbf{d}_0 = (\mathbf{L}_0^\dagger\mathbf{L}_0)^{-1}\tilde{\mathbf{m}}_0 = \mathbf{H}_0^{-1}\tilde{\mathbf{m}}_0, \\ \hat{\mathbf{m}}_1 &= (\mathbf{L}_1^\dagger\mathbf{L}_1)^{-1}\mathbf{L}_1^\dagger\mathbf{d}_1 = (\mathbf{L}_1^\dagger\mathbf{L}_1)^{-1}\tilde{\mathbf{m}}_1 = \mathbf{H}_1^{-1}\tilde{\mathbf{m}}_1, \end{aligned} \quad (4)$$

where $\tilde{\mathbf{m}}_0$ and $\tilde{\mathbf{m}}_1$ are the migrated baseline and monitor images, $\hat{\mathbf{m}}_0$ and $\hat{\mathbf{m}}_1$ are the inverted images, \mathbf{L}_0^\dagger and \mathbf{L}_1^\dagger are the migration operators (adjoints to the modeling

operators \mathbf{L}_0 and \mathbf{L}_1 respectively), and $\mathbf{H}_0 \equiv \mathbf{L}_0^\dagger \mathbf{L}_0$ and $\mathbf{H}_1 \equiv \mathbf{L}_1^\dagger \mathbf{L}_1$, are the Hessian matrices. Here, and in other parts of the paper, the symbol \dagger denotes transposed complex conjugate. Note that all discussions in this paper are based on (but not limited to) one-way wave-equation migration methods.

The Hessian matrices are the second derivatives of the cost functions (equation 9) with respect to all model points in the image. Further discussion on the wave-equation Hessian is given in the the next section and more detailed treatments of its derivation are found in Plessix and Mulder (2002), Mulder and Plessix (2004), and Valenciano et al. (2006). Because the Hessian matrices are generally not invertible for almost any practical scenario, equation 4 is solved iteratively as follows:

$$\begin{aligned} \mathbf{H}_0 \hat{\mathbf{m}}_0 &= \tilde{\mathbf{m}}_0, \\ \mathbf{H}_1 \hat{\mathbf{m}}_1 &= \tilde{\mathbf{m}}_1. \end{aligned} \quad (5)$$

An inverted time-lapse image, $\Delta \hat{\mathbf{m}}$, can be obtained as difference between the two images, $\hat{\mathbf{m}}_1$ and $\hat{\mathbf{m}}_0$, obtained from equation 5:

$$\Delta \hat{\mathbf{m}} = \hat{\mathbf{m}}_1 - \hat{\mathbf{m}}_0. \quad (6)$$

Computing the time-lapse image using equation 6 is regarded as *separate inversion* in other parts of this paper.

Joint Inversion

Another approach is to express the inversion as a single problem, in which both the baseline and time-lapse images are estimated simultaneously. We write the data modeling operation as follows:

$$\begin{aligned} \mathbf{L}_0 \mathbf{m}_0 &= \mathbf{d}_0, \\ \mathbf{L}_1 (\mathbf{m}_0 + \Delta \mathbf{m}) &= \mathbf{d}_1, \end{aligned} \quad (7)$$

where $\mathbf{m}_0 + \Delta \mathbf{m} = \mathbf{m}_1$. In matrix form, we can combine these expressions to write

$$\begin{bmatrix} \mathbf{L}_0 & \mathbf{0} \\ \mathbf{L}_1 & \mathbf{L}_1 \end{bmatrix} \begin{bmatrix} \mathbf{m}_0 \\ \Delta \mathbf{m} \end{bmatrix} = \begin{bmatrix} \mathbf{d}_0 \\ \mathbf{d}_1 \end{bmatrix}. \quad (8)$$

In principle, using an iterative solver, we can solve for the least-squares solution to equation 8 by minimizing the cost function

$$S(\mathbf{m}_0, \Delta \mathbf{m}) = \left\| \begin{bmatrix} \mathbf{L}_0 & \mathbf{0} \\ \mathbf{L}_1 & \mathbf{L}_1 \end{bmatrix} \begin{bmatrix} \mathbf{m}_0 \\ \Delta \mathbf{m} \end{bmatrix} - \begin{bmatrix} \mathbf{d}_0 \\ \mathbf{d}_1 \end{bmatrix} \right\|^2. \quad (9)$$

The cost of this approach is proportional to the number of iterations times twice the cost of one set of migrations — since one iteration requires one modeling and one migration for the baseline and monitor datasets. Since several iterations would

typically be required to reach convergence, and the inversion process would usually be repeated several times to fine-tune inversion parameters, the overall cost of this scheme may be considerably high. One advantage of the method discussed in the remaining part of this section is that modifications can be made to inversion parameters and the inversion repeated several times without the need for new migration or modeling. The least-squares solution to equation 8 is given by

$$\begin{bmatrix} \mathbf{L}_0^\dagger \mathbf{L}_0 + \mathbf{L}_1^\dagger \mathbf{L}_1 & \mathbf{L}_1^\dagger \mathbf{L}_1 \\ \mathbf{L}_1^\dagger \mathbf{L}_1 & \mathbf{L}_1^\dagger \mathbf{L}_1 \end{bmatrix} \begin{bmatrix} \hat{\mathbf{m}}_0 \\ \Delta \hat{\mathbf{m}} \end{bmatrix} = \begin{bmatrix} \mathbf{L}_0^\dagger & \mathbf{L}_1^\dagger \\ \mathbf{0} & \mathbf{L}_1^\dagger \end{bmatrix} \begin{bmatrix} \mathbf{d}_0 \\ \mathbf{d}_1 \end{bmatrix} = \begin{bmatrix} \tilde{\mathbf{m}}_0 + \tilde{\mathbf{m}}_1 \\ \tilde{\mathbf{m}}_1 \end{bmatrix}, \quad (10)$$

or

$$\begin{bmatrix} \mathbf{H}_0 + \mathbf{H}_1 & \mathbf{H}_1 \\ \mathbf{H}_1 & \mathbf{H}_1 \end{bmatrix} \begin{bmatrix} \hat{\mathbf{m}}_0 \\ \Delta \hat{\mathbf{m}} \end{bmatrix} = \begin{bmatrix} \tilde{\mathbf{m}}_0 + \tilde{\mathbf{m}}_1 \\ \tilde{\mathbf{m}}_1 \end{bmatrix}. \quad (11)$$

This can be re-casted as

$$\begin{bmatrix} \hat{\mathbf{m}}_0 \\ \Delta \hat{\mathbf{m}} \end{bmatrix} = \begin{bmatrix} \mathbf{H}_0 + \mathbf{H}_1 & \mathbf{H}_1 \\ \mathbf{H}_1 & \mathbf{H}_1 \end{bmatrix}^{-1} \begin{bmatrix} \tilde{\mathbf{m}}_0 + \tilde{\mathbf{m}}_1 \\ \tilde{\mathbf{m}}_1 \end{bmatrix}. \quad (12)$$

Thus, the inverted baseline and time-lapse images ($\hat{\mathbf{m}}_0$ and $\Delta \hat{\mathbf{m}}$ respectively) can be obtained from equation 12. As earlier noted, the Hessian matrices \mathbf{H}_0 and \mathbf{H}_1 (and hence the joint deconvolution operator) are not invertible, equation 11 must be solved iteratively.

In most TLSM problems, the general geology and reservoir architecture of the study area are known — thus providing some information that can be used to determine appropriate regularization for the inversion. Such regularization incorporates prior knowledge of the reservoir geometry and location, and expectation of changes in different parts of the study area. For example, equation 12 can be extended to include such prior information, to give

$$\begin{bmatrix} \mathbf{H}_0 + \mathbf{H}_1 & \mathbf{H}_1 \\ \mathbf{H}_1 & \mathbf{H}_1 \\ \epsilon_0 \mathbf{\Lambda}_0 \mathbf{R}_0 & \mathbf{0} \\ -\epsilon_1 \mathbf{\Lambda}_1 \mathbf{R}_0 & \epsilon_1 \mathbf{\Lambda}_1 \mathbf{R}_1 \end{bmatrix} \begin{bmatrix} \hat{\mathbf{m}}_0 \\ \Delta \hat{\mathbf{m}}_1 \end{bmatrix} = \begin{bmatrix} \tilde{\mathbf{m}}_0 + \tilde{\mathbf{m}}_1 \\ \tilde{\mathbf{m}}_1 \\ \mathbf{0} \\ \mathbf{0} \end{bmatrix}, \quad (13)$$

where, \mathbf{R}_0 and \mathbf{R}_1 are the spatial regularization terms for the baseline and time-lapse images respectively, $\mathbf{\Lambda}_0$ and $\mathbf{\Lambda}_1$ are temporal regularization (or coupling) between the surveys, while ϵ_0 and ϵ_1 determine strength of the regularization on the baseline and time-lapse images. The spatial and coupling operators can be applied over one or several dimensions (e.g., stacked-image, subsurface offset, or subsurface opening-angles), depending on the problem size, computational domain and a priori information available. While the spatial regularization operator contains information on the structural geometry of the reservoir (or implied properties of correctly migrated gathers, e.g. horizontal angle gathers, or near-zero concentration of amplitudes in subsurface offset gathers), the temporal regularization ensures that the reservoir changes evolve relatively smoothly. The temporal regularization term is similar to that used in the

so-called spatio-temporal tomographic inversion demonstrated by Ajo-Franklin et al. (2005).

We have extended this development to include additional surveys using the same procedure above (see Appendix A). For example, for three surveys (one baseline and two monitors), we can obtain the time-lapse images from

$$\begin{bmatrix} \mathbf{H}_0 + \mathbf{H}_1 + \mathbf{H}_2 & \mathbf{H}_1 + \mathbf{H}_2 & \mathbf{H}_2 \\ \mathbf{H}_1 + \mathbf{H}_2 & \mathbf{H}_1 + \mathbf{H}_2 & \mathbf{H}_2 \\ \mathbf{H}_2 & \mathbf{H}_2 & \mathbf{H}_2 \end{bmatrix} \begin{bmatrix} \hat{\mathbf{m}}_0 \\ \Delta \hat{\mathbf{m}}_1 \\ \Delta \hat{\mathbf{m}}_2 \end{bmatrix} = \begin{bmatrix} \tilde{\mathbf{m}}_0 + \tilde{\mathbf{m}}_1 + \tilde{\mathbf{m}}_2 \\ \tilde{\mathbf{m}}_1 + \tilde{\mathbf{m}}_2 \\ \tilde{\mathbf{m}}_2 \end{bmatrix}, \quad (14)$$

and including a regularization operator, we have

$$\begin{bmatrix} \mathbf{H}_0 + \mathbf{H}_1 + \mathbf{H}_2 & \mathbf{H}_1 + \mathbf{H}_2 & \mathbf{H}_2 \\ \mathbf{H}_1 + \mathbf{H}_2 & \mathbf{H}_1 + \mathbf{H}_2 & \mathbf{H}_2 \\ \mathbf{H}_2 & \mathbf{H}_2 & \mathbf{H}_2 \\ \hline \epsilon_0 \Lambda_0 \mathbf{R}_0 & \mathbf{0} & \mathbf{0} \\ -\epsilon_1 \Lambda_1 \mathbf{R}_0 & \epsilon_1 \Lambda_1 \mathbf{R}_1 & \mathbf{0} \\ \mathbf{0} & -\epsilon_2 \Lambda_2 \mathbf{R}_0 & \epsilon_2 \Lambda_2 \mathbf{R}_1 \end{bmatrix} \begin{bmatrix} \hat{\mathbf{m}}_0 \\ \Delta \hat{\mathbf{m}}_1 \\ \Delta \hat{\mathbf{m}}_2 \end{bmatrix} = \begin{bmatrix} \tilde{\mathbf{m}}_0 + \tilde{\mathbf{m}}_1 + \tilde{\mathbf{m}}_2 \\ \tilde{\mathbf{m}}_1 + \tilde{\mathbf{m}}_2 \\ \tilde{\mathbf{m}}_2 \\ \hline \mathbf{0} \\ \mathbf{0} \\ \mathbf{0} \end{bmatrix}. \quad (15)$$

Conceptually, equation A-7 can be useful in cases where several relatively small or sparse surveys, with different geometries are conducted at relatively short intervals, as proposed for example in the seismic monitoring of CO_2 sequestration (Arogunmati and Harris, 2007). We note that because different surveys would have some coincident shot or receiver locations, the overall computational cost of the Hessian (see next section) for different surveys is reduced.

Target-oriented Hessian

The cost of computing the full Hessian matrices (\mathbf{H}_1 to \mathbf{H}_N) in equation A-7 is prohibitive and not practical for almost any reasonably sized survey. Several authors (Shin et al., 2001; Rickett, 2003; Guitton, 2004; Valenciano et al., 2006; Symes, 2008) discussed common approximations to the Hessian. Also, schemes such as the random-phase and plane-wave encoding of the source and receiver Green's functions (Tang, 2008) ensure highly efficient approximate Hessian computation. In this paper, we follow the target-oriented approach of Valenciano et al. (2006).

Under the Born approximation, the synthetic seismic data, $\mathbf{d}(\mathbf{s}, \mathbf{r}; \omega)$ at a given frequency, ω , recorded by receiver $\mathbf{r}(x_r, y_r, z_r)$, from a shot $\mathbf{s}(x_s, y_s, z_s)$ and scattering point $\mathbf{x}(x, y, z)$, is given by

$$\mathbf{d}(\mathbf{s}, \mathbf{r}; \omega) = \omega^2 \sum_{\mathbf{x}} f(s) \mathbf{G}(\mathbf{x}, \mathbf{s}; \omega) \mathbf{G}(\mathbf{x}, \mathbf{r}; \omega) \mathbf{m}(\mathbf{x}), \quad (16)$$

where $f(s)$ is the source function, $\mathbf{G}(\mathbf{x}, \mathbf{s}; \omega)$ and $\mathbf{G}(\mathbf{x}, \mathbf{r}; \omega)$ are the Green's functions from the shot and receiver positions to the image point \mathbf{x} , with reflectivity $\mathbf{m}(\mathbf{x})$. Equation 16 describes the linear modeling process in equation 9.

The adjoint of the modeling operation in equation 16 is termed migration, which expressed in shot-profile formulation is

$$\mathbf{m}(\tilde{\mathbf{x}}) = \sum_w \omega^2 \sum_s f^\dagger(s) \mathbf{G}^\dagger(\mathbf{x}, \mathbf{s}; \omega) \sum_r \mathbf{G}^\dagger(\mathbf{x}, \mathbf{r}; \omega) \mathbf{d}(\mathbf{s}, \mathbf{r}; \omega), \quad (17)$$

where $\mathbf{m}(\tilde{\mathbf{x}})$ is the migrated image. The migration operator is equivalent to the negative gradient of the least-squares cost function (Tarantola, 1987) defined in equation 9, while the Hessian is (Plessix and Mulder, 2002; Valenciano et al., 2006)

$$\mathbf{H}(\mathbf{x}, \mathbf{y}) = \sum_w \omega^4 \sum_s |f^\dagger(s)|^2 \mathbf{G}^\dagger(\mathbf{x}, \mathbf{s}; \omega) \mathbf{G}(\mathbf{y}, \mathbf{s}; \omega) \sum_r \mathbf{G}^\dagger(\mathbf{x}, \mathbf{r}; \omega) \mathbf{G}(\mathbf{y}, \mathbf{r}; \omega), \quad (18)$$

where $\mathbf{y}(x, y, z)$ corresponds to all model points.

In order to explicitly compute the Hessian using equation 18, Green's functions from the surface shot and receiver positions to all image points need to be computed. The post-stack Hessian matrix is of size $N_x \times N_y \times N_z$ by $N_x \times N_y \times N_z$, where N_i is the number of image points along the i -axis. Including secondary dimensions such as the subsurface offsets or the subsurface opening-angle, the cost of computing equation 18 increases considerably (in proportion to the number of components along such dimension). It is not practicable to compute or store such a matrix, even for small surveys.

Because reservoirs typically are limited in extent, the region of interest is usually smaller than the full image space. The target-oriented approach (Valenciano et al., 2006) involves an explicit computation of Green's and the Hessian for a specific area of interest and for only a limited number of off-diagonal elements, (i.e., points around any image point). This method also takes into account the sparsity and structure of the Hessian, as well as particular acquisition geometry to greatly reduce the computational cost of the Hessian.

The target-oriented approach reduces equation 18 to

$$\mathbf{H}(\mathbf{x}_T, \mathbf{x}_T + \mathbf{a}_x) = \sum_w \omega^4 \sum_s |f^\dagger(s)|^2 \mathbf{G}^\dagger(\mathbf{x}_T, \mathbf{s}; \omega) \mathbf{G}(\mathbf{x}_T + \mathbf{a}_x, \mathbf{s}; \omega) \sum_r \mathbf{G}^\dagger(\mathbf{x}_T, \mathbf{r}; \omega) \mathbf{G}(\mathbf{x}_T + \mathbf{a}_x, \mathbf{r}; \omega), \quad (19)$$

where \mathbf{a}_x is the offset from the target image-point \mathbf{x}_T defining the deconvolution filter size and hence the number of off-diagonal terms to be computed. The filter size \mathbf{a}_x can be determined heuristically or from an analysis of the amplitudes of filter coefficients away from the diagonal. As noted by Valenciano (2008), the frequency sampling required to prevent wrap-around artifacts for the local filter (or row of the Hessian) for a given image point is coarser than that used in migration. This further reduces the overall computational cost of equation 19. Examples of the target-oriented Hessian for models in Figures 1 and 2 for two and three surveys are shown in Figures 3 and 4.

In a single survey, each row of the Hessian is a convolution filter (or point-spread function) describing the effects of the limited-bandwidth seismic waveform, geometry

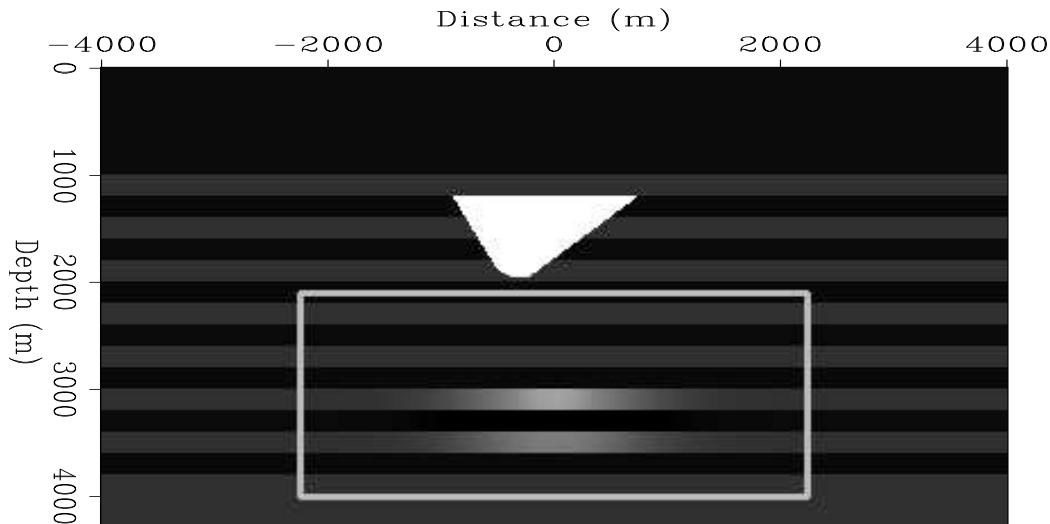


Figure 1: Full velocity model. The box indicates target area for which Figures 3 and 4 were computed, while the anomaly centered at distance 0m and depth 3000m represents the approximate location of reservoir change. The triangular block is a salt with velocity 4500m/s, while the surrounding sediments have alternating velocity of 2500m/s and 2700m/s. The densities range from 2.5g/cc to 3.0g/cc. [ER]

and illumination on a reflectivity spike in the subsurface. In multiple surveys, each band belonging to individual sub-matrices contains similar information from a single or combination of surveys as shown in equation A-7. Given the block and sparse matrix structure, we can use fast mathematical formulations specifically designed for such systems. Also, note that the empty bins in Figures 3 and 4 are neither computed nor stored and that because of the matrix symmetry, only one-half of it needs to be computed. The structure of the problem gives a large leeway for parallelization over several domains in the Hessian computation and inversion. Finally, since we assume that there is not a significant variation in the background velocity between surveys, and since some shot and receiver locations would be re-occupied during the monitor survey(s), the Green's functions can be reused. In the following sections, we demonstrate this inversion approach and compare results with those obtained using two approximations to the Hessian.

NUMERICAL EXAMPLES

We simulated changes in the reservoir properties (resulting from production) at different times during the production cycle as an increasing Gaussian anomaly centered at $x = 0\text{m}$ and $z = 3000\text{m}$ for the 2D model shown in Figure 1. The modeling parameters for the two survey geometries considered are summarized in Table 1.

The baseline survey was modeled with geometry A, while two monitors were modeled (for the same time-period) using geometries A and B. In all

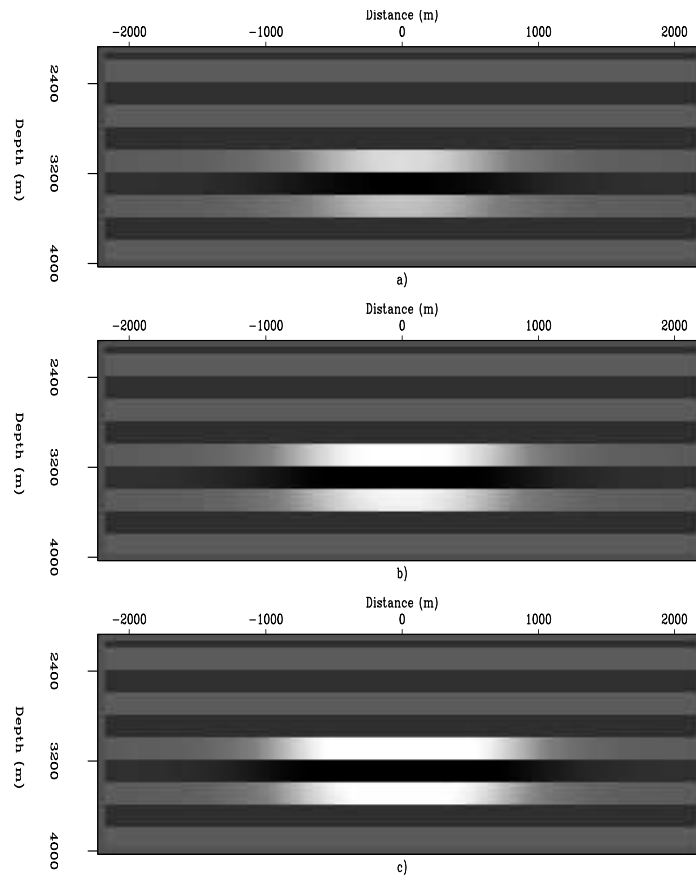


Figure 2: Reservoir models for the (a) baseline, (b) monitor, and (c) monitor 2 conditions around target area (distance, $x = -2200$ to $2200m$ and depth, $z = 2500$ to $4000m$). It is assumed that the reflectivity increases with time due to production. [ER]

Figure 3: Joint target-oriented Hessian for two surveys (one baseline and one monitor) for the subsalt reservoir models in Figure 1. The dimension of the square matrix here and in Figure 4 is equal to the number of surveys times the size of the model space. This figure corresponds to the operator in equation 12. Note however that the zeros (light regions in the matrices) were neither computed nor stored. [CR]

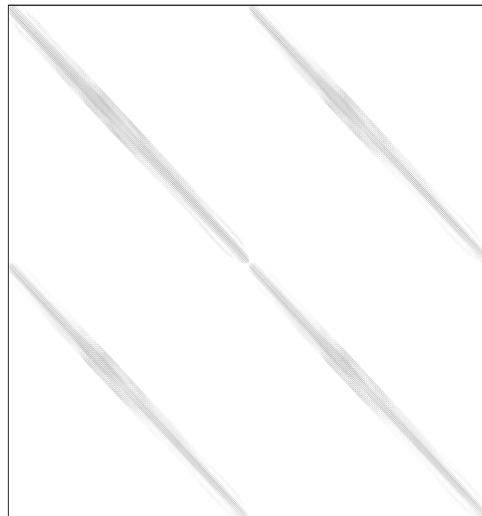


Figure 4: Joint target-oriented Hessian for one baseline and two monitor surveys for the reservoir models in Figure 1. See caption in Figure 3 for further description. [CR]

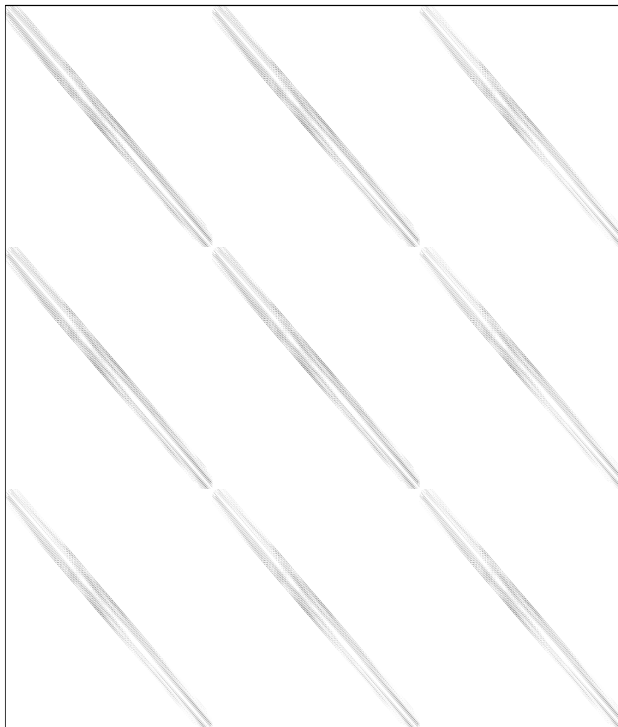


Table 1: Modeling parameters for synthetic datasets

	Geometry A	Geometry B
No. of shots	91	91
No. of receivers	271	271
Shot/receiver depth	0m	200m
Shot spacing	60m	60m
Receiver spacing	20m	20m
Shot/receiver spread	-2700 to 2700m	-3000 to 2400m

examples considered, the receiver spread is kept constant while the shots moves along. Also, we consider that reflectivity change is most influenced by a change in the density within the reservoir and that there is not a significant change in the background velocity model between surveys. This is needed in order to keep reflectors at lower depths than the reservoir top from significantly changing positions after migration with the baseline velocity.

The illumination maps (the diagonal of the Hessian) for both survey geometries are shown in Figure 6, while the migrated baseline and monitor images are shown in Figure 5. Note the irregular illumination pattern in Figure 6, which explain the uneven amplitudes of reflectors below the salt in Figure 5. The migrated results in this paper are obtained using a one-way shot-profile migration code. In the following sections we summarize some of the important results from the numerical tests.

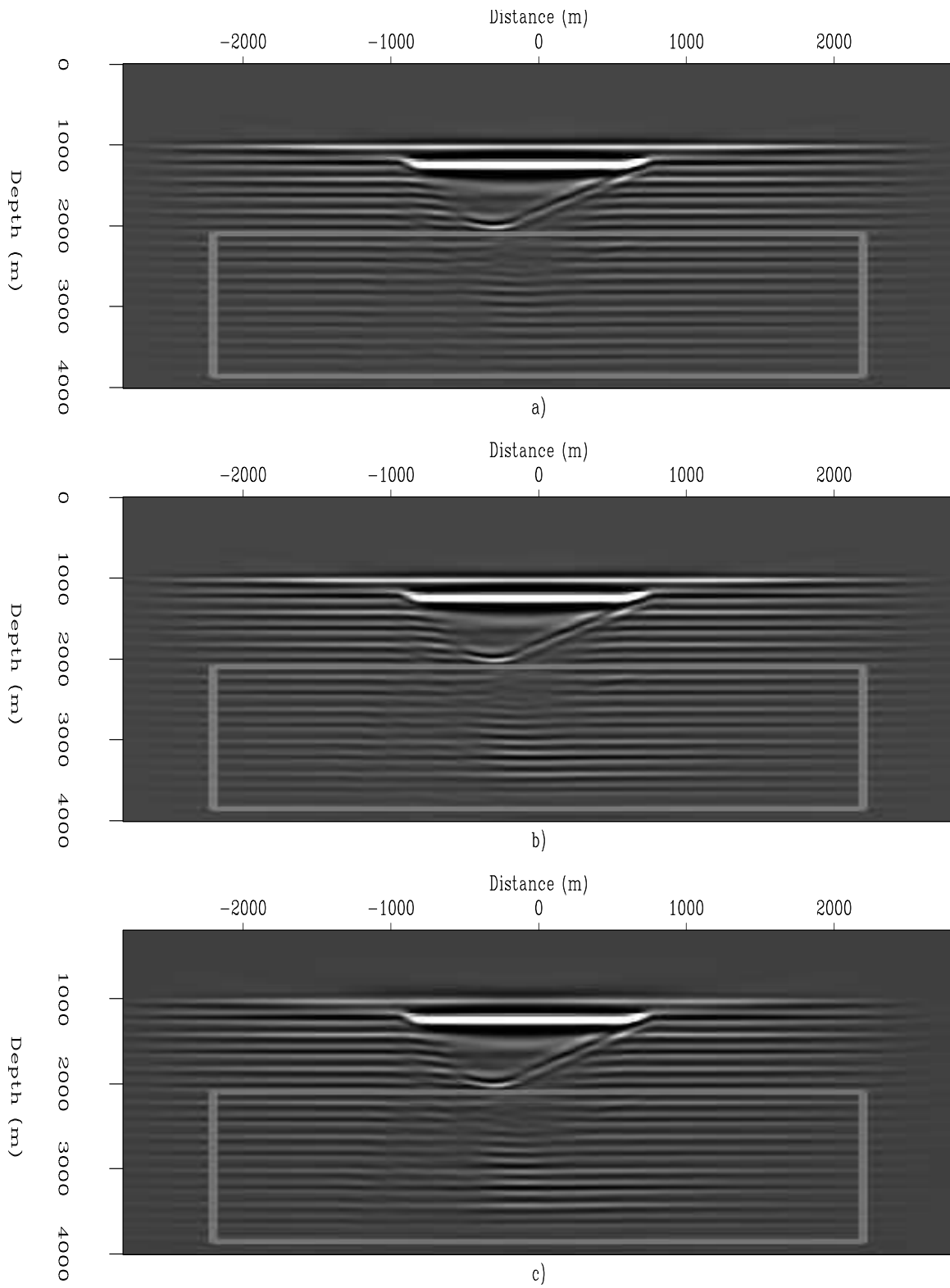


Figure 5: Migrated images for the (a) baseline, and monitor surveys with (b) same geometry as baseline, (c) different geometry from baseline. Note the irregular amplitude pattern below the salt structure. The box indicates the target area. [CR]

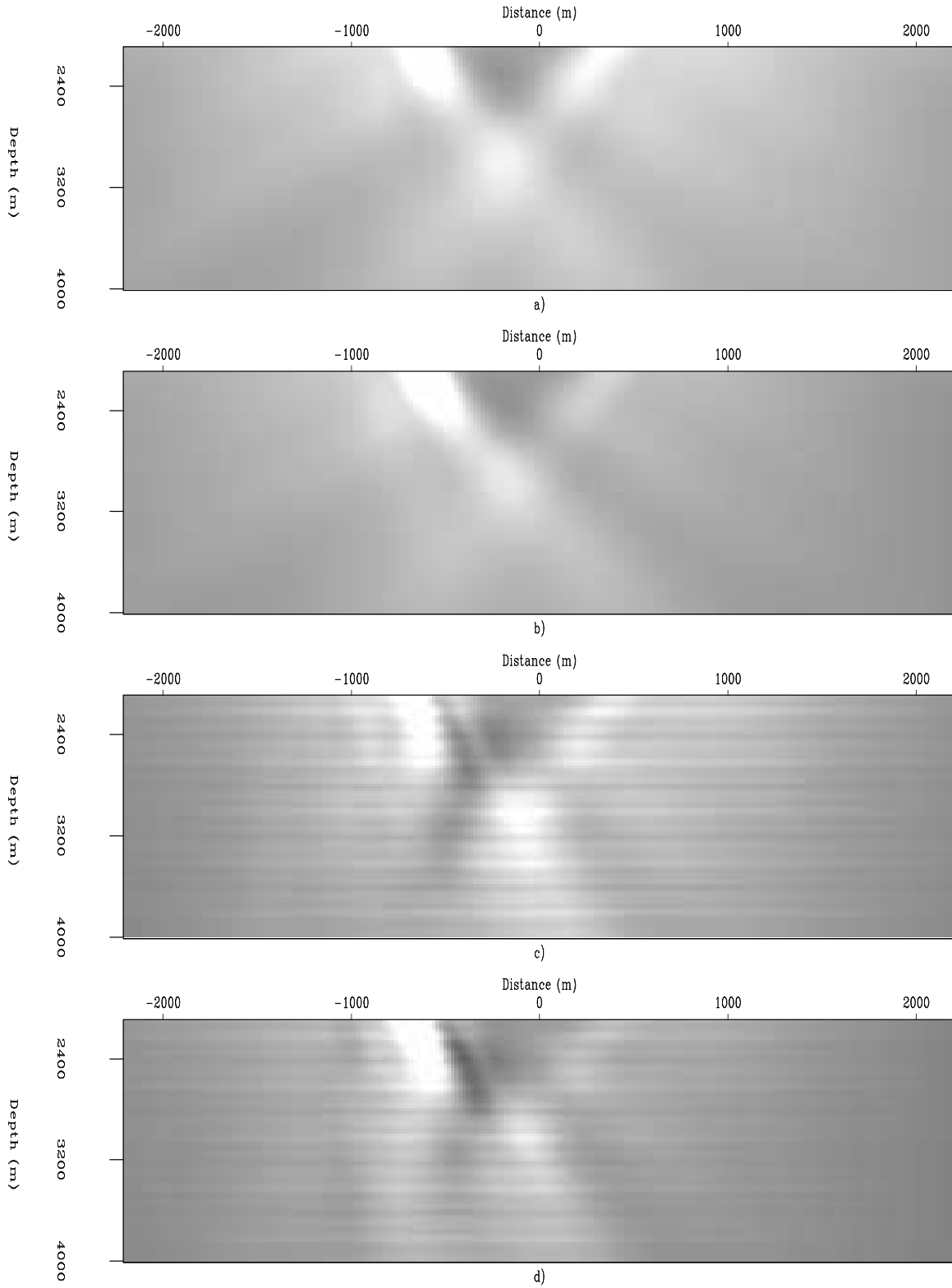


Figure 6: Illumination maps: (a) and (b) are the diagonal of the Hessian for the two geometries (A and B respectively) described in the text. (c) and (d) are respectively, the mass-lumped approximations to the Hessian (derived by summing a few off-diagonal terms in the Hessian into its diagonal) for geometries A and B. The light colors indicate high and the dark low illumination. [CR]

Synthetic I: Born data

To demonstrate the methodology for noise-free datasets where all events are completely defined by the one-way wave-equation, we simulated single scattering (Born) datasets for the baseline and monitor surveys. Because this is equivalent to the convolution of the one-way Hessian with the subsurface reflectivity, the wave-propagation and scattering are completely defined by the the Hessian. Figure 7 shows time-lapse images obtained from shot-profile migration and inversion, while Figure 8 shows a comparison of the time-lapse amplitudes along the top of the reservoir (at depth $z = 3000\text{m}$). For comparison, we include the time-lapse images obtained by weighting the migrated images with the diagonal of the Hessian (Duquet et al., 2000) and with a mass-lumped approximation (Chavent and Plessix, 1999) in both Figures 7 and 8. Only one inversion result is shown in both figures as the separate and joint inversions yield exactly the same result. With a different monitor geometry, B , the inversion goals are simultaneous corrections for both the illumination and geometry artifacts. Figures 9 and 10 show the corresponding the time-lapse results obtained using different geometries for the two surveys.

Next, we investigate the effect of uncorrelated noise on both the separate and joint inversion schemes, since in practice the migrated image is not entirely noise-free. We added different levels of uniformly-distributed random noise to the migrated images and try to invert the using the same operators as those in the noise-free case. The inversion results from this exercise are presented in Figure 11. Note that for different amount of noise in the migrated images, the separately inverted time-lapse images are consistently higher than those obtained from joint inversion.

Synthetic II: Two-way modeling

We modeled synthetic two-way data with a time-domain variable density acoustic wave-equation. Since one-way operators were used in the computation of the Green's functions, the Hessian contains no information regarding secondary events such as multiples. No pre-processing was done to remove multiples from the data and hence we expect these to have some impact on the inversion. For perfectly repeated surveys (i.e., using geometry A for both baseline and monitor surveys), the time-lapse images obtained from differences of migrated images, weighted migrated images (using diagonal of the Hessian and the mass-lumped approximation), and inversion are shown in Figure 12. Both the separate and joint inversion results were obtained with regularization incorporating structural information of the reservoir. Note that there is little improvement in the joint inversion result over separate inversion. With non-repeated survey geometries (i.e. geometry A for the baseline and B for the monitor survey), the images obtained from migration, weighted migration and inversion are shown in Figure 13. Note that the image from joint inversion has less artifacts compared than other methods.

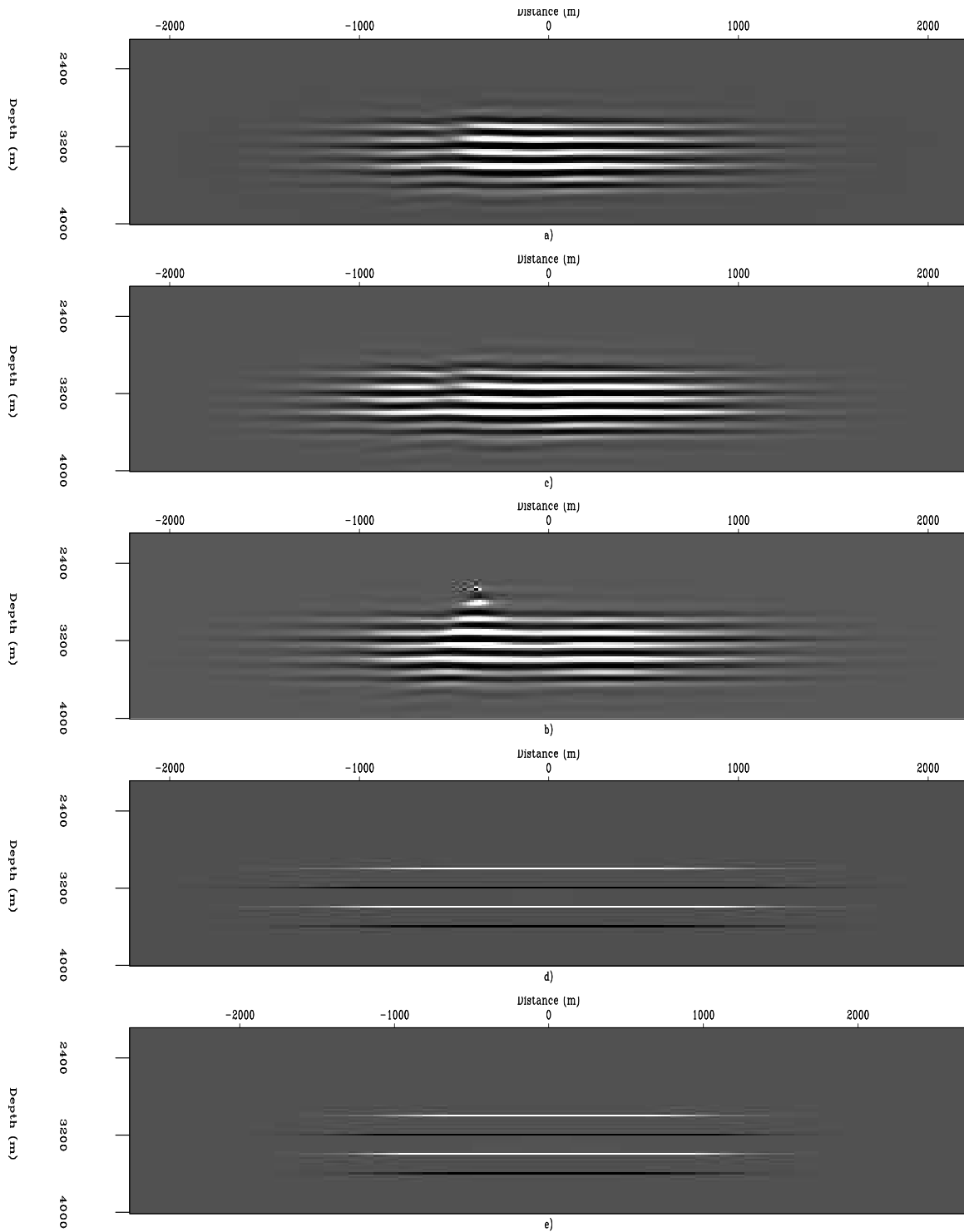


Figure 7: Time-lapse reflectivity amplitudes for perfectly repeated surveys derived from (a) migration, migration weighted by the (b) diagonal of the Hessian, and (c) diagonal matrix from the mass-lumping approximation. (d) shows the image difference from joint inversion — result from separate inversion is not show because the results are the same as joint inversion— and (e) is the true reflectivity change. [CR]

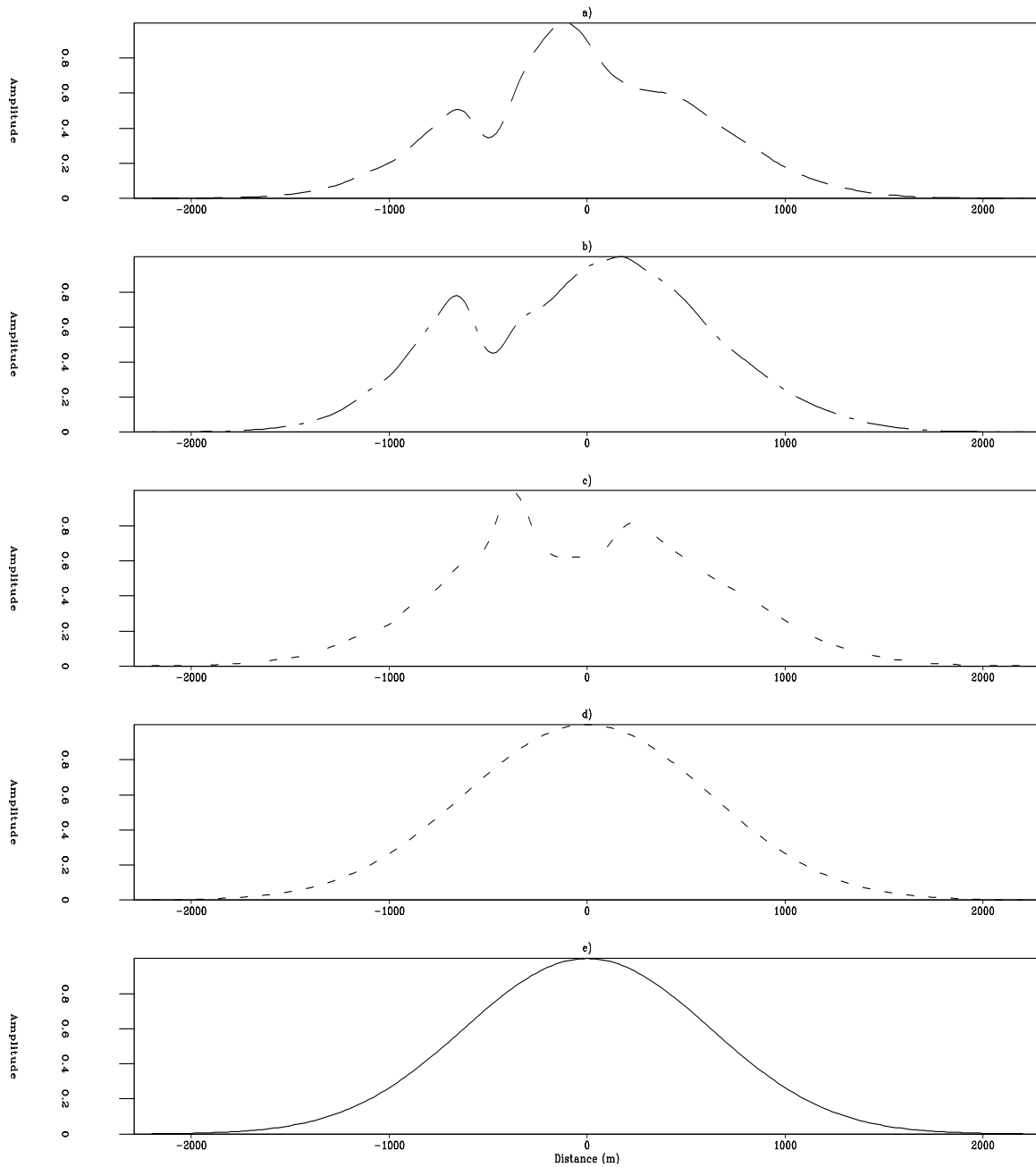


Figure 8: Normalized time-lapse amplitudes above the reservoir (depth 3000m) for perfectly repeated surveys. Each plot corresponds to the images in Figure 7. Note that in the migrated and weighted images, the reflectivity change is strongly distorted and that inversion perfectly reproduces the true reflectivity change. [CR]

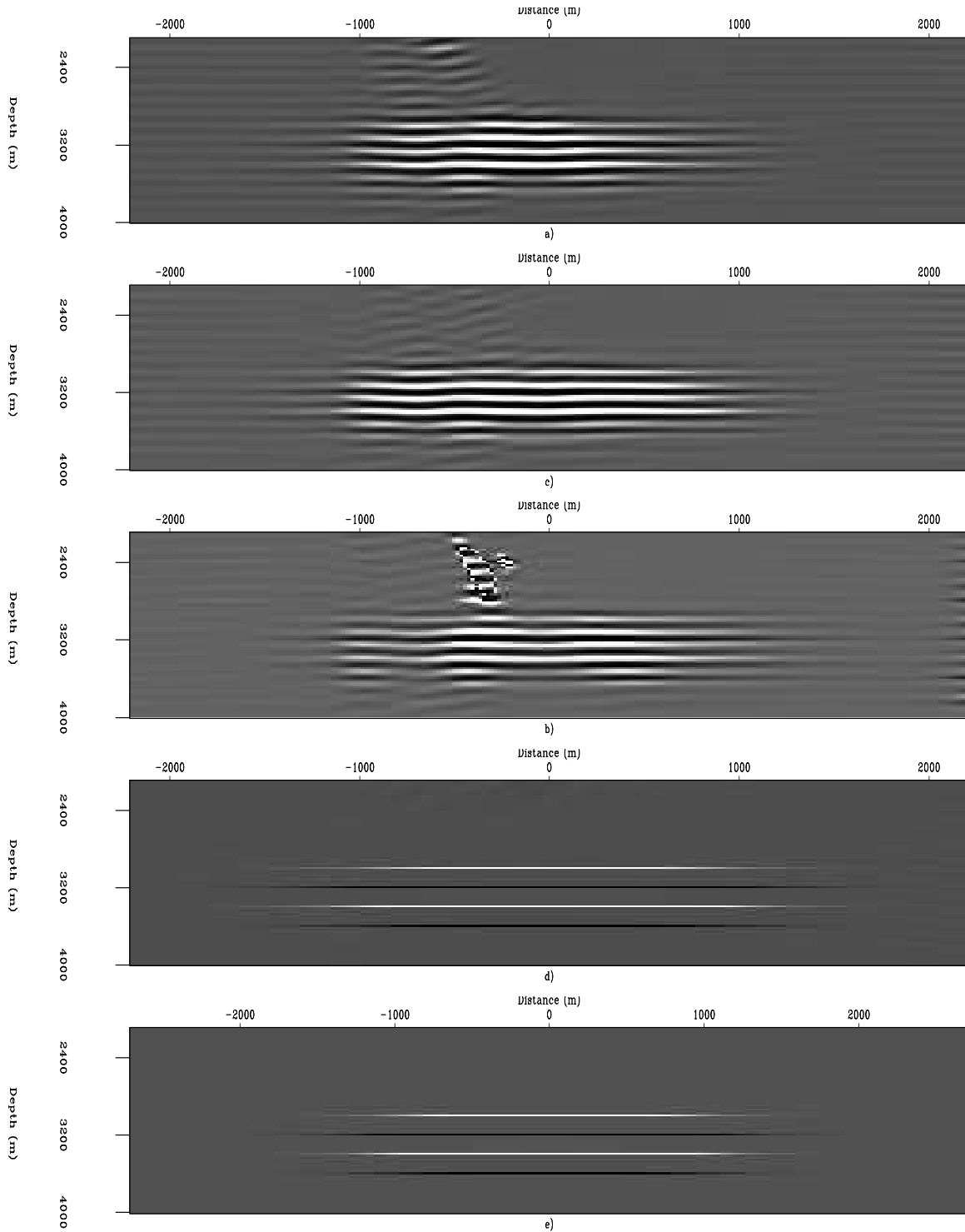


Figure 9: Time-lapse reflectivity amplitudes for different baseline and monitor geometries. See caption in Figure 7. By comparing (a) to Figure 7a, note that above the reservoir, there is a large image difference caused by both uneven illumination and the different survey geometries. Also note the poor performance of the diagonal weighting in (b) and (c), compared with inversion (d), which perfectly reproduces the true reflectivity change shown in (e). [CR]

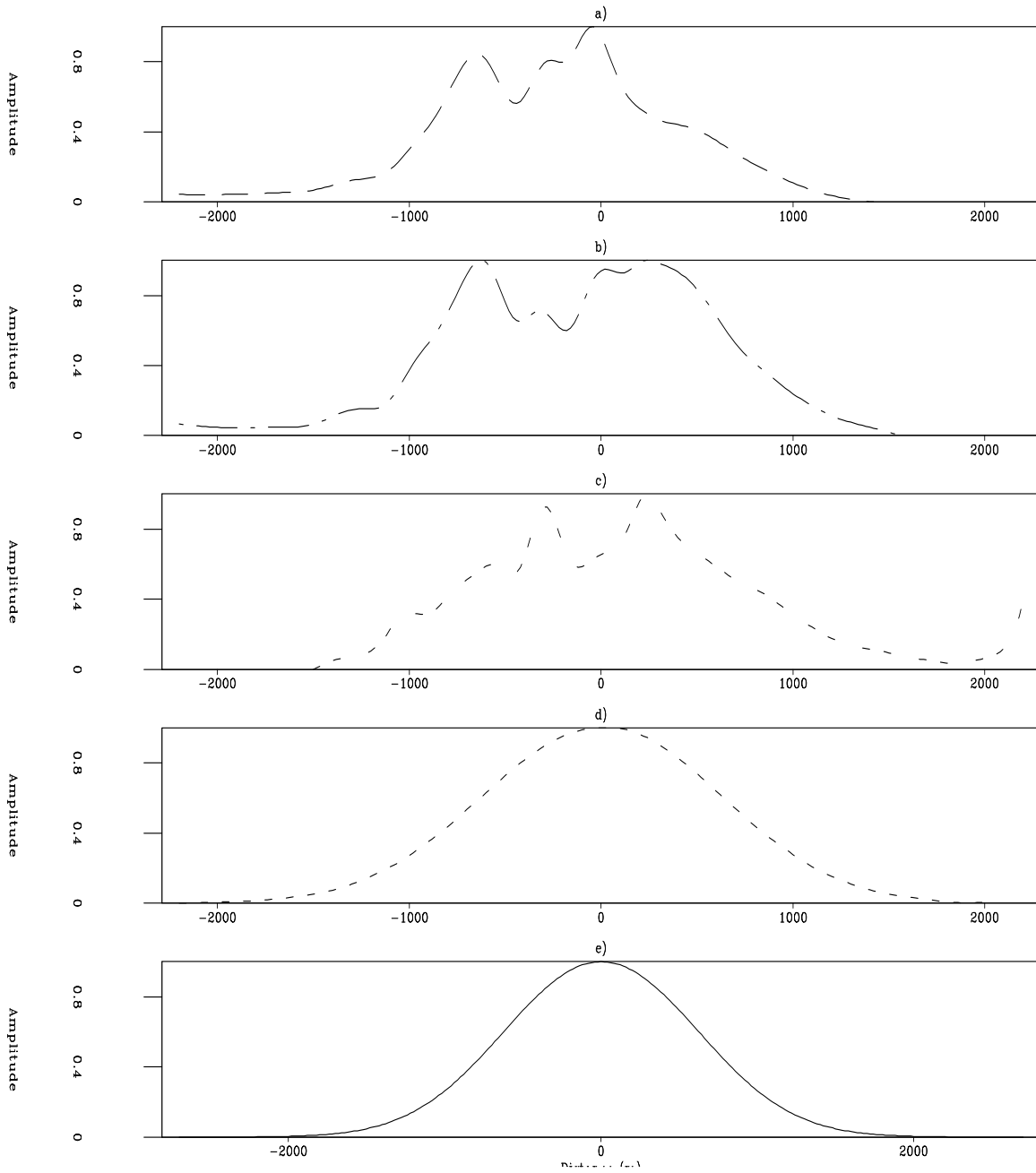


Figure 10: Normalized time-lapse amplitudes at top of the reservoir, (depth 3000m) for perfectly repeated surveys. Each plot corresponds to the images in Figures 9. Compare these to Figures 8. Note that in the migrated and weighted images, the reflectivity change is distorted and that inversion perfectly reproduces the true reflectivity change. [CR]

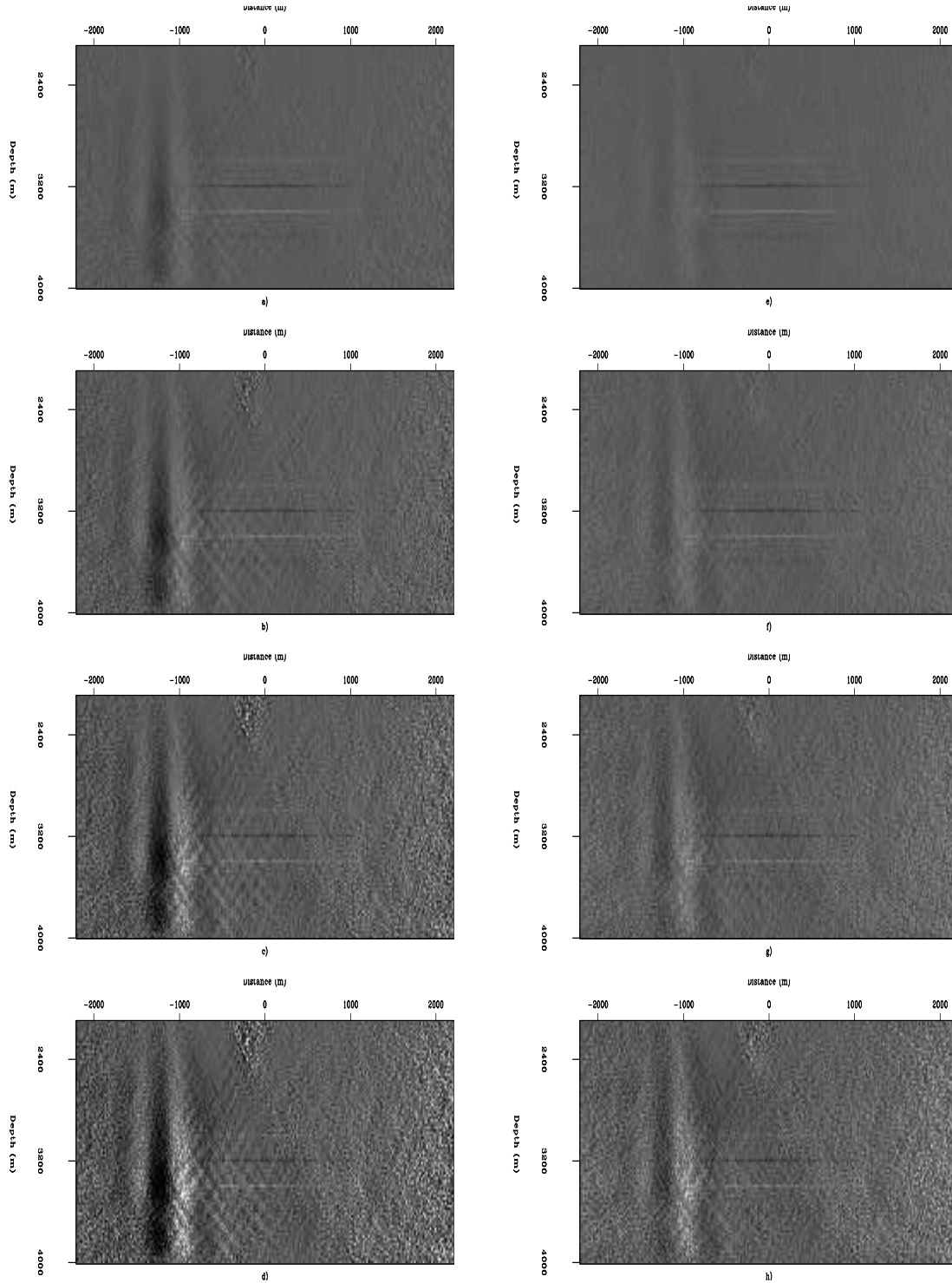


Figure 11: Time-lapse images obtained from separate, (a) - (d) and joint, (e) - (h) inversion with different (from top, 2.5, 5.0, 7.5, and 10.0%) levels of uniform random noise added to the migrated images. The baseline and monitor surveys were modeled with the different geometries (A and B respectively). Note that the noise level is higher in the separately inverted images relative to the jointly inverted images ones, especially in parts of the model with poor illumination. [CR]

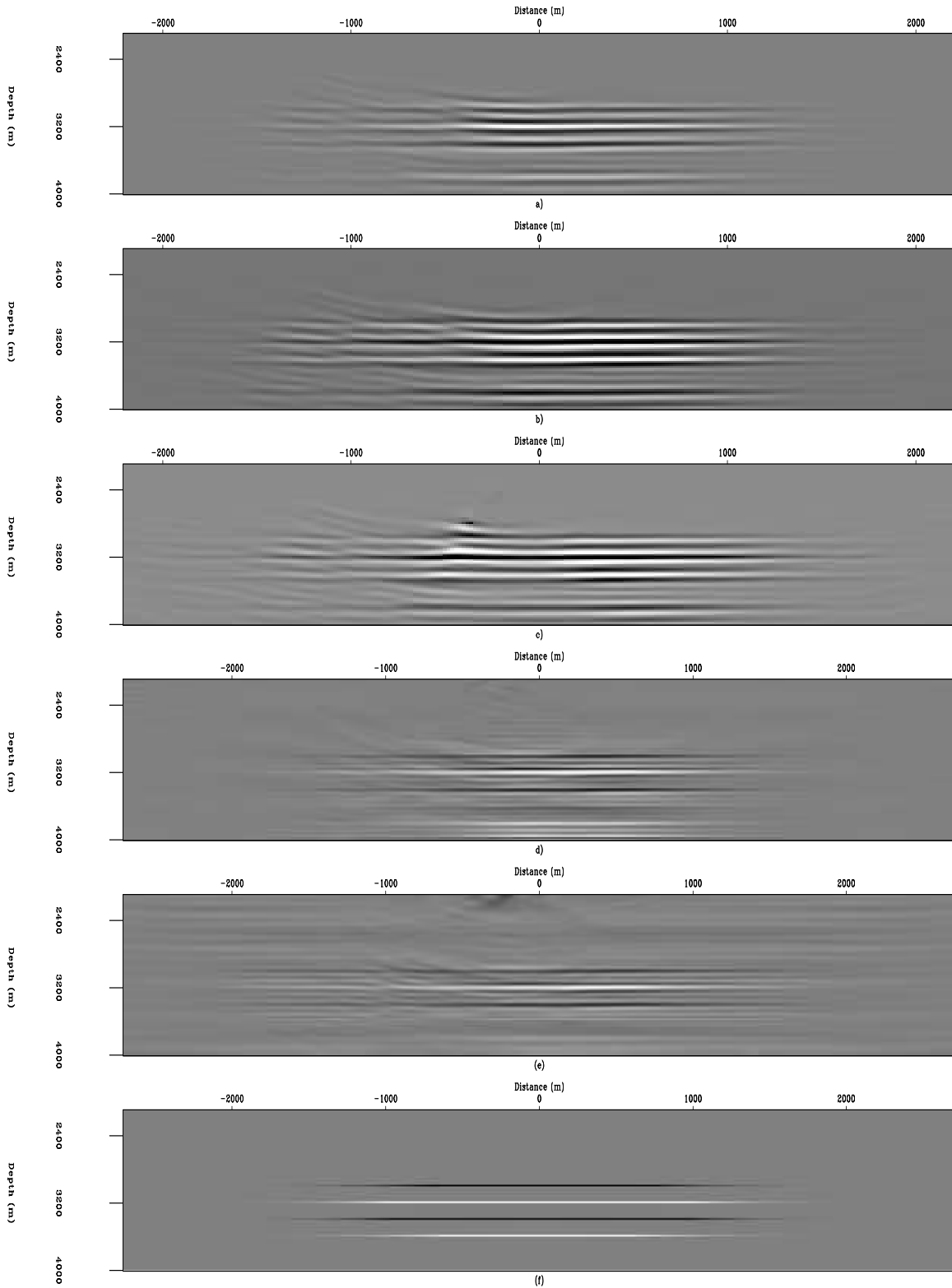


Figure 12: Time-lapse reflectivity for perfectly repeated survey geometries. The images are derived from (a) migration, weighted migrated images using the (b) diagonal, and (c) mass-lumping approximation, (d) separate inversion, (e) joint inversion, and (f) is the true reflectivity change. [CR]

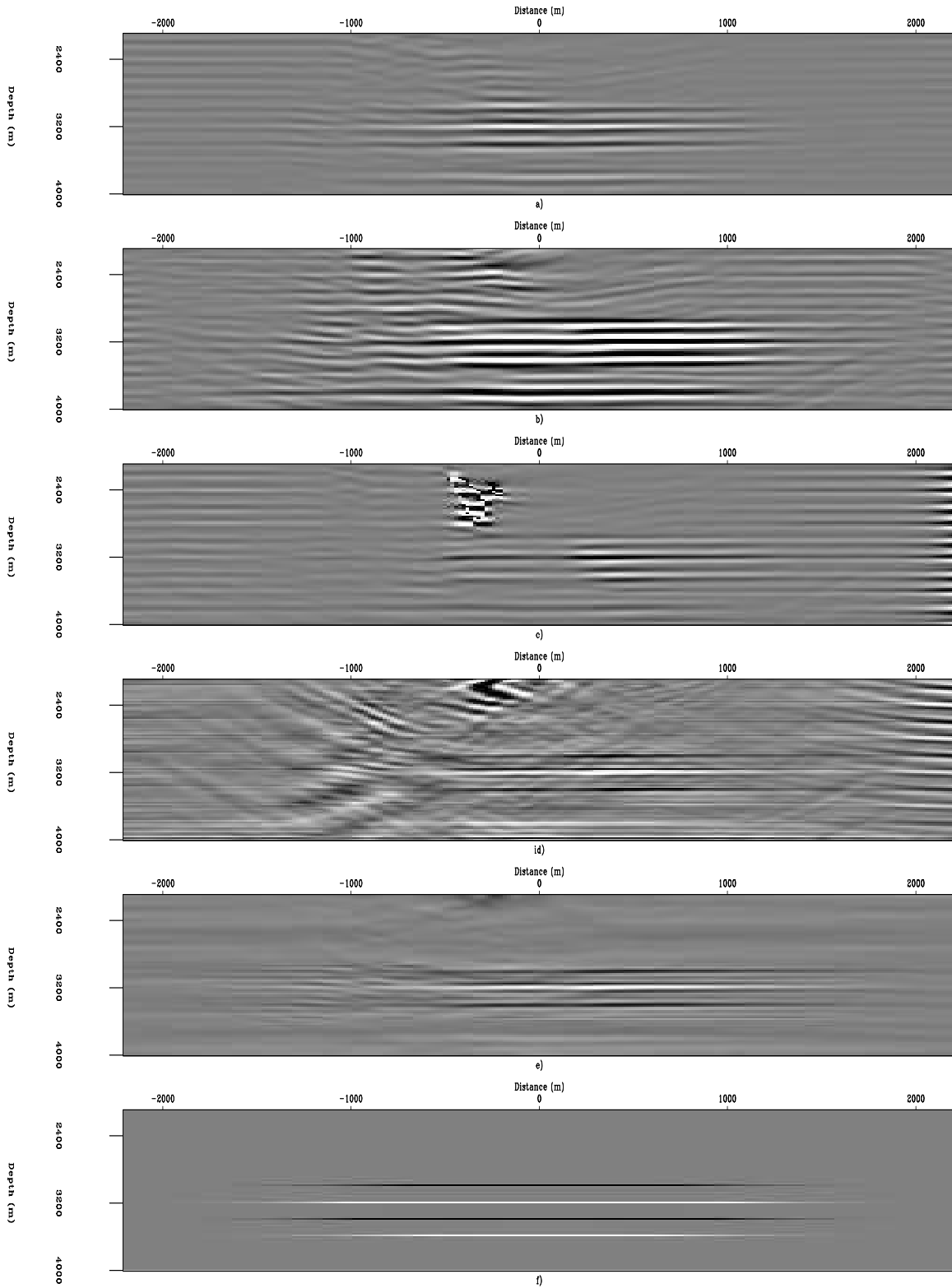


Figure 13: Time-lapse reflectivity using different survey geometries for baseline (geometry A) and monitor (geometry B). The images were derived from (a) migration, weighted migrated images using the (b) diagonal, and (c) mass-lumping approximation, (d) separate inversion, (e) joint inversion, and (f) is the true reflectivity change. [CR]

DISCUSSION

Results from inversion of the Born datasets suggest that it is possible to recover the true time-lapse reflectivity if the Hessian accurately models the propagation and scattering of waves in seismic experiments. As shown in Figures 7 and 8, the images recovered from weighting migrated images with either the diagonal of the Hessian or its mass-lumped equivalent are inferior to those from inversion. This is because these weights contain no information regarding the shape of the filter, resulting from the finite frequency of the seismic waveform, direction of illumination and local dips of reflectors — information captured in the off-diagonal elements of the target-oriented filter used in the inversion. The limitation of such weights become even more apparent when the survey geometries are not repeated as shown in Figures 9 and 10, where the inversion recovers the true reflectivity change but the weighting operators perform poorly. In the absence of noise both separate and joint inversion yield comparable results; however with uncorrelated random noise present the joint inversion yields superior images as shown in Figure 11. An intuitive explanation for such improvement is that by using a combination of operators over the same model, the overall effect of the noise would reduce, since the iterative search becomes more robust. The inversion results from the two-way data shows the improvement derivable from both separate and joint inversion as shown in Figures 12 and 13. Note that, though there is limited improvement in the joint inversion image relative to that from separate inversion when the geometries are the same (Figures 12d and e), there is remarkable improvement over separate inversion when the geometries are different as shown in Figures 13d and e. Weighting operators (e.g. diagonal of the Hessian, a mass-lumping, or other approximation) are an over-simplification of the inversion and therefore yield inaccurate results as shown in Figures 13b and c. As shown in all the inverted images, the seismic wavelet has been deconvolved from the time-lapse, thus increasing the resolution.

CONCLUSIONS

Seismic monitoring of reservoirs under complex overburden is challenging due to a combination of factors including uneven illumination and non-repeatability of acquisition geometries. We have proposed a joint inversion scheme to solve both the imaging and monitoring problems typical of such complex geological environments. The numerical examples show that we can address illumination and geometry problems, that cause contamination the time-lapse seismic responses below complex overburden. We speculate this scheme could make reservoir monitoring in subsalt (and other complex) reservoirs feasible. This scheme is also more robust than migration and inversion using the most common approximations to the Hessian. In the presence of random uncorrelated noise, this inversion scheme would yield better results than separately inverting the migrated images. We concede that the overall cost of the Hessian is still outside reach for most reasonably large surveys, but by using the target-oriented approach discussed in the paper, particular areas of interest can be sufficiently handled.

We do believe that with new computational methods such as phase- or plane-wave encoding, increased computational speed and storage capacity of computers, and the need to monitor reservoirs in complex frontiers, the joint inversion method proposed here would become practical. Finally, although separate inversion is computationally less expensive, joint inversion provides more flexibility in model styling/regularization during inversion.

ACKNOWLEDGMENTS

The first author acknowledges contributions from Alejandro Valenciano and Yaxun Tang, whose previous and current research have helped him through understanding wave-equation inversion and efficient computational methods for the Hessian. Discussions with Bob Clapp and Claudio Cardoso helped shape this research.

REFERENCES

- Ajo-Franklin, J. B., J. Urban, and J. M. Harris, 2005, Temporal integration of seismic traveltimes tomography: SEG Technical Program Expanded Abstracts, **24**, 2468–2471.
- Arogunmati, A. and J. Harris, 2007, Data integration for spatiotemporal imaging.
- Batzle, M. and Z. Wang, 1992, Seismic properties of pore fluids: *Geophysics*, **57**, 1396–1408.
- Calvert, R., 2005, Insights and methods for 4D reservoir monitoring and characterization: SEG/EAGE DISC (Distinguished Instructor Lecture Course).
- Chavent, G. and R. E. Plessix, 1999, An optimal true-amplitude least-squares prestack depth-migration operator: *Geophysics*, **64**, 508–515.
- Duquet, B., K. J. Marfurt, and J. Dellinger, 2000, Kirchhoff modeling, inversion for reflectivity, and subsurface illumination: *Geophysics*, **65**, 1195–1209.
- Eastwood, J., P. Lebel, A. Dilay, and S. Blakeslee, 1994, Seismic monitoring of steam-based recovery of bitumen: *The Leading Edge*, **13**, 242–251.
- Eiken, O., G. U. Haugen, M. Schonewille, and A. Duijndam, 2003, A proven method for acquiring highly repeatable towed streamer seismic data: *Geophysics*, **68**, 1303–1309.
- Guitton, A., 2004, Amplitude and kinematic corrections of migrated images for nonunitary imaging operators: *Geophysics*, **69**, 1017–1024.
- Johnston, D., 2005, Time-lapse 4D technology: Reservoir surveillance: AAPG Search and Discovery.
- Korneev, V. and A. Bakulin, 2006, On the fundamentals of the virtual source method: *Geophysics*, **71**, A13–A17.
- Laws, R. and E. Kragh, 2000, Rough seas and time-lapse seismic: 62nd Mtg., Session:L0015, Eur. Assn. Geosci. Eng.
- Lefeuvre, F., Y. Kerdraon, J. Peliganga, S. Medina, P. Charrier, R. L’Houtellier, and D. Dubucq, 2003, Improved reservoir understanding through rapid and effective 4D: Girassol field, Angola, West Africa: SEG Technical Program Expanded Abstracts, **22**, 1334–1337.
- Lumley, D. E., 1995, Seismic time-lapse monitoring of subsurface fluid flow: PhD thesis, Stanford University, <http://sepwww.stanford.edu/public/docs/sep91/>.
- Muerdter, D. and D. Ratcliff, 2001, Understanding subsalt illumination through ray-trace modeling, Part 3: Salt ridges and furrows, and the impact of acquisition orientation: *The Leading Edge*, **20**, 803–816.
- Mulder, W. and R.-E. Plessix, 2004, Frequency-domain finite-frequency amplitude-preserving migration: *Geophysical Journal International*, **157**, 975–985.
- Plessix, R.-E. and W. Mulder, 2002, Amplitude-preserving finite-difference migration based on a least-squares formulation in the frequency domain: SEG Technical Program Expanded Abstracts, **21**, 1212–1215.
- Rickett, J., 2003, Illumination-based normalization for wave-equation depth migration: *Geophysics*, **68**, 1371–1379.
- Rickett, J. and D. E. Lumley, 2001, Cross-equalization data processing for time-lapse seismic reservoir monitoring: A case study from the Gulf of Mexico: *Geophysics*,

- 66**, 1015–1025.
- Ross, C. P. and M. S. Altan, 1997, Time-lapse seismic monitoring: Some shortcomings in nonuniform processing: *The Leading Edge*, **16**, 931–937.
- Sarkar, S., W. P. Gouveia, and D. H. Johnston, 2003, On the inversion of time-lapse seismic data: *SEG Technical Program Expanded Abstracts*, **22**, 1489–1492.
- Sava, P., 2006, Subsalt exploration and development: Imaging, interpretation, and drilling—what have we learned? 2006 SEG/EAGE summer research workshop: *The Leading Edge*, **25**, 1370–1376.
- Shin, C., S. Jang, and D.-J. Min, 2001, Improved amplitude preservation for prestack depth migration by inverse scattering theory: *Geophysical Prospecting*, **49**, 592–606.
- Symes, W. W., 2008, Approximate linearized inversion by optimal scaling of prestack depth migration: *Geophysics*, **73**, R23–R35.
- Tang, Y., 2008, Wave-equation hessian by phase encoding: SEP-134.
- Tarantola, A., 1987, *Inverse problem theory: Methods for data fitting and model parameter estimation*: Elsevier Science Publication Company, Inc.
- Valenciano, A., 2008, *Imaging by Wave-Equation Inversion*: PhD thesis, Stanford University.
- Valenciano, A. A., B. Biondi, and A. Guitton, 2006, Target-oriented wave-equation inversion: *Geophysics*, **71**, A35–A38.
- Whitcombe, D. N., J. M. Marsh, P. J. Clifford, M. Dyce, C. J. S. McKenzie, S. Campbell, A. J. Hill, R. S. Parr, C. Pearse, T. A. Ricketts, C. P. Slater, and O. L. Barkved, 2004, The systematic application of 4D in BP’s North-West Europe operations — 5 years on: *SEG Technical Program Expanded Abstracts*, **23**, 2251–2254.
- Zhang, M., M. D. Sacchi, and D. R. Schmitt, 2005, Simultaneous inversion of time-lapse seismic data: *CSEG Conference*, 228–231.
- Zou, Y., L. R. Bentley, L. R. Lines, and D. Coombe, 2006, Integration of seismic methods with reservoir simulation, Pikes Peak heavy-oil field, Saskatchewan: *The Leading Edge*, **25**, 764–781.

APPENDIX A

JOINT INVERSION FORMULATION FOR MULTIPLE SURVEYS

This appendix shows an extension of the joint inversion formulation to an arbitrary number of surveys. For three surveys, the data modeling procedure is given by

$$\begin{bmatrix} \mathbf{L}_0 & \mathbf{0} & \mathbf{0} \\ \mathbf{L}_1 & \mathbf{L}_1 & \mathbf{0} \\ \mathbf{L}_2 & \mathbf{L}_2 & \mathbf{L}_2 \end{bmatrix} \begin{bmatrix} \mathbf{m}_0 \\ \Delta\mathbf{m}_1 \\ \Delta\mathbf{m}_2 \end{bmatrix} = \begin{bmatrix} \mathbf{d}_0 \\ \mathbf{d}_1 \\ \mathbf{d}_2 \end{bmatrix}, \quad (\text{A-1})$$

where \mathbf{d}_0 , \mathbf{d}_1 and \mathbf{d}_2 are respectively datasets for the baseline, first and second monitor, \mathbf{m}_0 is the baseline reflectivity and the time-lapse reflectivities $\Delta\mathbf{m}_1$ and $\Delta\mathbf{m}_2$ are defined as

$$\begin{aligned} \Delta\mathbf{m}_1 &= \mathbf{m}_1 - \mathbf{m}_0, \\ \Delta\mathbf{m}_2 &= \mathbf{m}_2 - \mathbf{m}_1, \end{aligned} \quad (\text{A-2})$$

where \mathbf{m}_1 and \mathbf{m}_2 are respectively the monitor reflectivities at the times data \mathbf{d}_0 and \mathbf{d}_1 were acquired (with survey geometries defined by the linear \mathbf{L}_1 and \mathbf{L}_2). The least-squares solution to equation A-1 is given as:

$$\begin{bmatrix} \mathbf{L}_0^\dagger\mathbf{L}_0 + \mathbf{L}_1^\dagger\mathbf{L}_1 + \mathbf{L}_2^\dagger\mathbf{L}_2 & \mathbf{L}_1^\dagger\mathbf{L}_1 + \mathbf{L}_2^\dagger\mathbf{L}_2 & \mathbf{L}_2^\dagger\mathbf{L}_2 \\ \mathbf{L}_1^\dagger\mathbf{L}_1 + \mathbf{L}_2^\dagger\mathbf{L}_2 & \mathbf{L}_1^\dagger\mathbf{L}_1 + \mathbf{L}_2^\dagger\mathbf{L}_2 & \mathbf{L}_2^\dagger\mathbf{L}_2 \\ \mathbf{L}_2^\dagger\mathbf{L}_2 & \mathbf{L}_2^\dagger\mathbf{L}_2 & \mathbf{L}_2^\dagger\mathbf{L}_2 \end{bmatrix} \begin{bmatrix} \hat{\mathbf{m}}_0 \\ \Delta\hat{\mathbf{m}}_1 \\ \Delta\hat{\mathbf{m}}_2 \end{bmatrix} = \begin{bmatrix} \mathbf{L}_0^\dagger & \mathbf{L}_1^\dagger & \mathbf{L}_2^\dagger \\ & \mathbf{L}_1^\dagger & \mathbf{L}_2^\dagger \\ & & \mathbf{L}_2^\dagger \end{bmatrix} \begin{bmatrix} \mathbf{d}_0 \\ \mathbf{d}_1 \\ \mathbf{d}_2 \end{bmatrix}, \quad (\text{A-3})$$

where the symbol \dagger denotes transposed complex conjugate. We rewrite equation A-3 as

$$\begin{bmatrix} \mathbf{H}_0 + \mathbf{H}_1 + \mathbf{H}_2 & \mathbf{H}_1 + \mathbf{H}_2 & \mathbf{H}_2 \\ \mathbf{H}_1 + \mathbf{H}_2 & \mathbf{H}_1 + \mathbf{H}_2 & \mathbf{H}_2 \\ \mathbf{H}_2 & \mathbf{H}_2 & \mathbf{H}_2 \end{bmatrix} \begin{bmatrix} \hat{\mathbf{m}}_0 \\ \Delta\hat{\mathbf{m}}_1 \\ \Delta\hat{\mathbf{m}}_2 \end{bmatrix} = \begin{bmatrix} \tilde{\mathbf{m}}_0 + \tilde{\mathbf{m}}_1 + \tilde{\mathbf{m}}_2 \\ \tilde{\mathbf{m}}_1 + \tilde{\mathbf{m}}_2 \\ \tilde{\mathbf{m}}_2 \end{bmatrix}, \quad (\text{A-4})$$

where $\tilde{\mathbf{m}}_i$ is the migrated image from the i_{th} survey, and \mathbf{H}_i is the corresponding Hessian matrix. Introducing a styling/regularization term that incorporates prior knowledge of the reservoir geometry and location as well as constraints on the inverted time-lapse images into equation A-4 we obtain

$$\begin{bmatrix} \mathbf{H}_0 + \mathbf{H}_1 + \mathbf{H}_2 & \mathbf{H}_1 + \mathbf{H}_2 & \mathbf{H}_2 \\ \mathbf{H}_1 + \mathbf{H}_2 & \mathbf{H}_1 + \mathbf{H}_2 & \mathbf{H}_2 \\ \mathbf{H}_2 & \mathbf{H}_2 & \mathbf{H}_2 \\ \hline \epsilon_0\Lambda_0\mathbf{R}_0 & \mathbf{0} & \mathbf{0} \\ -\epsilon_1\Lambda_1\mathbf{R}_0 & \epsilon_1\Lambda_1\mathbf{R}_1 & \mathbf{0} \\ \mathbf{0} & -\epsilon_2\Lambda_2\mathbf{R}_0 & \epsilon_2\Lambda_2\mathbf{R}_1 \end{bmatrix} \begin{bmatrix} \hat{\mathbf{m}}_0 \\ \Delta\hat{\mathbf{m}}_1 \\ \Delta\hat{\mathbf{m}}_2 \end{bmatrix} = \begin{bmatrix} \tilde{\mathbf{m}}_0 + \tilde{\mathbf{m}}_1 + \tilde{\mathbf{m}}_2 \\ \tilde{\mathbf{m}}_1 + \tilde{\mathbf{m}}_2 \\ \tilde{\mathbf{m}}_2 \\ \hline \mathbf{0} \\ \mathbf{0} \\ \mathbf{0} \end{bmatrix}. \quad (\text{A-5})$$

With four surveys, the time-lapse images can be obtained by solving the equation

$$\begin{bmatrix} \mathbf{H}_0 + \mathbf{H}_1 + \mathbf{H}_2 + \mathbf{H}_3 & \mathbf{H}_1 + \mathbf{H}_2 + \mathbf{H}_3 & \mathbf{H}_2 + \mathbf{H}_3 & \mathbf{H}_3 \\ \mathbf{H}_1 + \mathbf{H}_2 + \mathbf{H}_3 & \mathbf{H}_1 + \mathbf{H}_2 + \mathbf{H}_3 & \mathbf{H}_2 + \mathbf{H}_3 & \mathbf{H}_3 \\ \mathbf{H}_2 + \mathbf{H}_3 & \mathbf{H}_2 + \mathbf{H}_3 & \mathbf{H}_2 + \mathbf{H}_3 & \mathbf{H}_3 \\ \mathbf{H}_3 & \mathbf{H}_3 & \mathbf{H}_3 & \mathbf{H}_3 \end{bmatrix} \begin{bmatrix} \hat{\mathbf{m}}_0 \\ \Delta \hat{\mathbf{m}}_1 \\ \Delta \hat{\mathbf{m}}_2 \\ \Delta \hat{\mathbf{m}}_3 \end{bmatrix} = \begin{bmatrix} \tilde{\mathbf{m}}_0 + \tilde{\mathbf{m}}_1 + \tilde{\mathbf{m}}_2 + \tilde{\mathbf{m}}_3 \\ \tilde{\mathbf{m}}_1 + \tilde{\mathbf{m}}_2 + \tilde{\mathbf{m}}_3 \\ \tilde{\mathbf{m}}_2 + \tilde{\mathbf{m}}_3 \\ \tilde{\mathbf{m}}_3 \end{bmatrix}, \quad (\text{A-6})$$

and for N surveys

$$\begin{bmatrix} \mathbf{H}_0 + \dots + \mathbf{H}_N & \mathbf{H}_1 + \dots + \mathbf{H}_N & \mathbf{H}_2 + \dots + \mathbf{H}_N & \dots & \mathbf{H}_N \\ \mathbf{H}_1 + \dots + \mathbf{H}_N & \mathbf{H}_1 + \dots + \mathbf{H}_N & \mathbf{H}_2 + \dots + \mathbf{H}_N & \dots & \mathbf{H}_N \\ \mathbf{H}_2 + \dots + \mathbf{H}_N & \mathbf{H}_2 + \dots + \mathbf{H}_N & \mathbf{H}_2 + \dots + \mathbf{H}_N & \dots & \mathbf{H}_N \\ \vdots & \vdots & \vdots & \vdots & \vdots \\ \vdots & \vdots & \vdots & \vdots & \vdots \\ \mathbf{H}_N & \mathbf{H}_N & \mathbf{H}_N & \dots & \mathbf{H}_N \end{bmatrix} \begin{bmatrix} \hat{\mathbf{m}}_0 \\ \Delta \hat{\mathbf{m}}_1 \\ \Delta \hat{\mathbf{m}}_2 \\ \vdots \\ \vdots \\ \Delta \hat{\mathbf{m}}_N \end{bmatrix} = \begin{bmatrix} \tilde{\mathbf{m}}_0 + \dots + \tilde{\mathbf{m}}_N \\ \tilde{\mathbf{m}}_1 + \dots + \tilde{\mathbf{m}}_N \\ \tilde{\mathbf{m}}_2 + \dots + \tilde{\mathbf{m}}_N \\ \vdots \\ \vdots \\ \mathbf{m}_N \end{bmatrix}. \quad (\text{A-7})$$

By solving equation A-7, it is possible to obtain the inverted baseline and time-lapse images from multiple surveys. We note that because different surveys would have some coincident shot or receiver locations computational cost of the Hessian for different surveys is reduced. Finally, introducing a regularization operator into equation A-7, the deconvolution operator becomes

$$\begin{bmatrix} \mathbf{H}_0 + \dots + \mathbf{H}_N & \mathbf{H}_1 + \dots + \mathbf{H}_N & \mathbf{H}_2 + \dots + \mathbf{H}_N & \dots & \mathbf{H}_N \\ \mathbf{H}_1 + \dots + \mathbf{H}_N & \mathbf{H}_1 + \dots + \mathbf{H}_N & \mathbf{H}_2 + \dots + \mathbf{H}_N & \dots & \mathbf{H}_N \\ \mathbf{H}_2 + \dots + \mathbf{H}_N & \mathbf{H}_2 + \dots + \mathbf{H}_N & \mathbf{H}_2 + \dots + \mathbf{H}_N & \dots & \mathbf{H}_N \\ \vdots & \vdots & \vdots & \vdots & \vdots \\ \vdots & \vdots & \vdots & \vdots & \vdots \\ \mathbf{H}_N & \mathbf{H}_N & \mathbf{H}_N & \dots & \mathbf{H}_N \\ \hline \epsilon_0 \Lambda_0 \mathbf{R}_0 & - & - & - & - \\ -\epsilon_1 \Lambda_1 \mathbf{R}_0 & \epsilon_1 \Lambda_1 \mathbf{R}_1 & - & - & - \\ - & -\epsilon_2 \Lambda_2 \mathbf{R}_1 & \epsilon_2 \Lambda_2 \mathbf{R}_2 & - & - \\ - & - & \vdots & \vdots & - \\ - & - & \vdots & \vdots & - \\ - & - & -\epsilon_{N-1} \Lambda_{N-1} \mathbf{R}_{N-2} & \epsilon_{N-1} \Lambda_{N-1} \mathbf{R}_{N-1} & - \\ - & - & - & -\epsilon_N \Lambda_N \mathbf{R}_{N-1} & \epsilon_N \Lambda_N \mathbf{R}_N \end{bmatrix}, \quad (\text{A-8})$$

where, \mathbf{R}_i is the spatial regularization for survey i , Λ_i is the temporal regularization between surveys, and ϵ_i determines the relative importance of model changes between surveys.